

## Magnetic Resonance Microscopy

### *Concepts, Challenges, and State-of-the-Art*

**Barjor Gimi**

#### Summary

Recent strides in targeted therapy and regenerative medicine have created a need to identify molecules and metabolic pathways implicated in a disease and its treatment. These molecules and pathways must be discerned at the cellular level to meaningfully reveal the biochemical underpinnings of the disease and to identify key molecular targets for therapy. Magnetic resonance (MR) techniques are well suited for molecular and functional imaging because of their noninvasive nature and their versatility in extracting physiological, biochemical, and functional information over time. However, MR is an insensitive technique; MR microscopy seeks to increase detection sensitivity, thereby localizing biochemical and functional information at the level of single cells or small cellular clusters. Here, we discuss some of the challenges facing MR microscopy and the technical and phenomenological strategies used to overcome these challenges. Some of the applications of MR microscopy are highlighted in this chapter.

**Key Words:** Magnetic resonance; Microimaging; Microcoil; Scroll coil; Microscopy; RF sensitivity; Signal-to-noise ratio (SNR).

#### 1. Introduction

Advances in genetics and bioengineering have inspired therapeutic approaches targeted at the cellular and molecular levels. Investigating how cellular pathways and manipulated cells interact with their environment *in vitro* and *in vivo*, their response to drugs and immune attack, and their viability over time requires tools that allow for long-term and noninvasive assessment. Magnetic resonance (MR) spatially correlates biochemical information, providing a context in which these issues may be addressed. Refinement of microfabrication and nanofabrication techniques, electronic circuitry, and pulse sequences has propelled MR toward the realm of microscopy. High-resolution *in vitro* and *in vivo* information on a biological system is instructive in study-

ing disease progression, regression, and aggressiveness, as well as the pH, oxygen tension, and energy status of cellular systems, metabolite levels, changes in their distribution in regions-of-interest, drug delivery, and the outcome of treatment.

The term ‘MR microscopy’ is loosely defined in the scientific literature. Traditionally, for *in vitro* systems, microscopy refers to voxels whose dimensions are on the order of tens of microns. *In vivo* systems entail a lower operating frequency, smaller magnetic gradients, and a less-sensitive detection system. Therefore, for *in vivo* systems, the term ‘microscopy’ applies to voxels whose dimensions are on the order of hundreds of microns. This nomenclature is not very revelatory. Assuming all observations are performed at a given field strength, the attainable voxel resolution depends on the time taken to acquire the signal. An insensitive system can provide high spatial resolution if the acquisition is long, whereas a comparatively sensitive system may provide lower spatial resolution if the acquisition is effectuated in a shorter time period. MR resolution is also a function of the nucleus/molecule being observed. Nuclei with higher magnetic receptivity (gyromagnetic ratio) will produce more signal; the more nuclei a given voxel contains, the higher the attainable signal from that voxel. To complicate matters further, MR observation is dependent on experimental parameters (e.g., pulse sequence and type of encoding system). Different pulse sequences and encoding systems tailored to observe specific phenomena, such as diffusion, perfusion, and compartmentalization, will yield different resolution. Thus, in light of these caveats, how one defines microscopy depends on what one wants to observe.

Although most principles governing conventional MR and MR microscopy are analogous, there are certain challenges distinct to microscopy. This chapter introduces the reader to microscopy—its salient concepts, its challenges, and its applications. The body of the chapter is divided into four sections. The first section deals with obtaining high-resolution data. The second examines phenomenological issues, classified as ‘broadening effects,’ which impede on or can be exploited in microscopy. Biological applications of microscopy are addressed in the third section. The final section explores future directions.

## **2. Challenges Facing MR Microscopy**

Three major components of an MRI acquisition system influence the image quality, namely signal-to-noise ratio (SNR), spatial resolution, and contrast. The field strength of the scanner, of course, is a crucial determinant of the signal strength. However, once field strength is fixed by choice of a scanner, the only other component available for the user to optimize further is the radio frequency (RF) excitation and receiver chain. Spatial resolution is determined

by the gradient system. This section will review the primary issues and strategies usually employed to address those issues. Also included is a discussion on different contrast mechanisms available.

## **2.1. Technical Strategies: RF Excitation and Reception**

A principal impediment in MR is low detection sensitivity, which is directly related to the signal strength and SNR. The objective in optimizing MRI sensitivity is to increase the signal strength while minimizing the noise contributions.

### **2.1.1. Improving Signal Strength**

MR is an insensitive technique because its signal depends on the population difference of nuclear spins in two energy states, which is on the order of mere parts per million. For instance, at room temperature and in a magnetic field of 1 T, only 6 of approx 2 million  $^1\text{H}$  nuclei contribute to the MR signal. The impediment of low signal is exacerbated at higher spatial resolution because a smaller voxel will contain proportionately fewer nuclear spins. Furthermore, acquisition time varies inversely with  $\text{SNR}^2$ . For a given detection sensitivity, improving spatial resolution by an order of magnitude in each Cartesian axis while keeping SNR the constant requires an acquisition time that is 1 million times longer. The task of improving resolution is daunting for  $^1\text{H}$ , which has high biological abundance and high magnetic receptivity, but when observing nuclei that are less abundant in the body and have low signal receptivity, such as  $^{13}\text{C}$  and  $^{31}\text{P}$ , the task becomes inordinately difficult. Therefore, technical efforts in MR microscopy are directed toward enhancing signal amplitude, reducing noise, and increasing detection sensitivity.

Signal amplitude may be increased by increasing the nuclear spin population differential between two energy states, one where the nucleus is parallel to the applied magnetic field and one where the nucleus is antiparallel to the applied magnetic field. An increase in this population difference can be achieved by increasing the strength of the applied static magnetic field, or by polarizing the sample. MR at high magnetic field strengths is desirable despite the significant expense and increased static field inhomogeneity associated with it. However, although SNR increases roughly linearly with static magnetic field strength, microscopy requires several orders of magnitude improvement in SNR over conventional MR. Signal enhancement is also achieved by polarizing the sample, which, in turn, increases the relative population of nuclear spins that contribute to the signal. The hyperpolarization technique is sometimes used in imaging airways and blood volume, but is often not physiologically possible or appropriate. However, recent studies show that hyperpolarized  $^{13}\text{C}$  can be used in medical applications, such as contrast-enhanced MR angiography (*I*).

### 2.1.2. Minimizing Noise Contributions

Another approach to increasing SNR is to decrease noise from both the spectrometer and the sample. Noise arising from the spectrometer can be reduced or eliminated using cryocooled probes and preamplifiers or high-temperature superconducting (HTS) RF coils (2–4). HTS coils appear to be the obvious choice for reducing the thermal noise, and have been used in loop transmission line and Helmholtz configurations, but they have a low usable bandwidth. Neglecting sample loading, HTS coils can achieve a Q-factor (i.e., the quality of a resonant system, defined as the resonant frequency divided by the bandwidth) increase of two to three orders of magnitude, at liquid nitrogen temperatures:

$$(SNR \propto \sqrt{Q}).$$

However, at temperatures where the sample becomes the dominant source of noise, supercooled conventional coils can yield SNR gains approaching those of HTS coils (5). Therefore, cooling conventional copper coils may be preferred from the standpoint of simplicity and cost. Although these noise reduction techniques have potential, they have yet to be refined to the point of implementation for widespread application. At present, engineering efforts to increase SNR are directed principally toward increasing RF sensitivity at room temperature by miniaturizing the RF coil.

### 2.1.3. Improving RF Sensitivity by Dedicated RF Coils

Designing a good RF circuit (**Fig. 1**) involves manufacturing a suitable RF coil, ensuring that signal emanating from the coil's electrical leads does not interfere with the image or spectrum quality, ensuring that no capacitors or other circuit elements resonate at the operating frequency, minimizing energy losses in the circuit, and impedance matching the sample–coil construct to the preamplifier for a continuous wave transmission to ensure maximum power transfer at resonance. The goal is to maximize SNR.

SNR is directly proportional to RF sensitivity and can be expressed as (6,7):

$$SNR \propto \frac{\omega_0^2 \cdot \left( \frac{B_1}{i} \right) \cdot V_s}{\sqrt{R_{noise}}},$$

where  $\omega_0$  is the resonance frequency,  $B_1/i$  is the coil sensitivity and is defined as the transverse magnetic field generated by the coil per unit current,  $V_s$  is the sample volume, and  $R_{noise}$  is the noise resistance from the sample and the coil. Sample resistive losses are negligible in the microcoil regime, and the total resistance is dominated by the coil resistance and  $R_{noise} \approx R_{microcoil}$  (8,9).

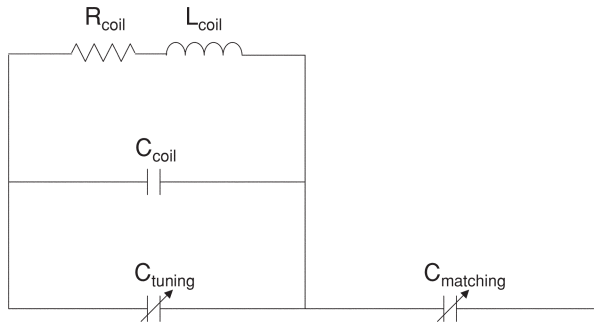


Fig. 1. A schematic of the radio frequency circuit. The coil can be modeled as a capacitor in parallel with an inductor and resistor. A capacitor in parallel with the coil is used for tuning the circuit, whereas a capacitor in series is used for impedance matching.

SNR can be increased by increasing the static field strength (thereby increasing  $\omega_0^2$ ), increasing the sample volume, increasing the coil sensitivity, and decreasing the noise. For a volume-limited sample,  $V_s$  cannot be altered but the effective sample volume can be increased by increasing the coil's filling factor such that the sample occupies most of the sensing region of the coil. For a given field strength, SNR increase is most expediently and effectively achieved by decreasing the coil size to match the sample size, thereby increasing the effective volume and the sensitivity. SNR improvements result in significant reduction in acquisition time and permit observation of physiological processes, and avoid prolonged anesthesia in *in vivo* studies. Therefore, coil miniaturization and geometric optimization are the foci of RF coil design for MR microscopy.

To address the sensitivity requirements of microscopy, a new generation of coils called 'microcoils' has been developed (10–14). Microcoils are loosely defined as coils whose sensing volume is less than 10  $\mu\text{L}$  (15). Microcoils have distinct challenges related to scalability issues. The coils must be mechanically stable, capable of incorporating the sample within their sensing volume, able to carry large currents, and able to dissipate heat without adverse effects on the sample.

As the conductor thickness and inter-turn separation (in the case of multi-turn microcoils) are reduced, eddy currents in the wire reduce its effective cross-section through skin effects and proximity effects. A high frequency alternating current (AC) generates eddy currents at the center of the wire, and the conductive current concentrates toward the wire perimeter, in a region characterized by skin depth,  $\delta$ . This results in losses beyond the resistive direct current (DC) losses. For multiturn microcoils, each turn of the microcoil generates

eddy currents in neighboring turns, resulting in an additional AC loss mechanism called ‘proximity loss.’ When the wire radius is equal to the skin depth, the cross-sectional current distribution is uniform, and closely approximates the DC case. Therefore, although one would ideally design microcoils with conductors several times thicker than the skin depth, limitations in fabrication techniques constrain conductor thickness to be close to the skin depth. In such a case, fabricating microcoils with a conductor thickness equal to twice the skin depth provides better performance than slightly thicker conductors, with a few provisos that are beyond the scope of this chapter (7).

Thus, there are competing geometry requirements for high microcoil performance. As the microcoil dimension decreases, inter-turn separation must decrease to provide a strong and homogeneous field. The reduced separation between turns results in additional proximity losses. We address these competing design requirements in our ensuing discussing of microcoil design. It should be noted that the microcoils discussed in this chapter are transceivers, i.e., the same microcoil is used to transmit power and receive signal. Therefore, better field characteristics in the microcoil’s transmission mode will result in increased sensitivity in its reception mode.

#### 2.1.3.1. VOLUME MICROCOILS

Volume coils are best suited for applications requiring high field homogeneity and for sample geometry that is primarily three-dimensional. Saddle, birdcage, and solenoid coils are typical (**Fig. 2**). This section will focus on the solenoid, a well studied and widely used microcoil, and the novel multilayered scroll microcoil that can increase SNR by incorporating several sensing layers.

Solenoid microcoils have been routinely fabricated by winding thin wire on a small-diameter capillary. A method for constructing solenoid microcoils is detailed below. A small-diameter, polyimide-coated, fused silica capillary is held in a pin vise, and a polyurethane-coated copper wire loop with a preload at both ends is suspended from the capillary and glued onto it with cyanoacrylate. The capillary should be free of contaminants and the adhesive must be used sparingly to avoid field distortions arising from susceptibility effects. Once the adhesive is bound, the preload at one end is removed and the coil is wound by rotating the pin vise to achieve the necessary solenoid. The wire at the other end of the solenoid is then glued, and the preload removed. The polyurethane coating is chemically etched or mechanically removed from the leads, the coil-capillary construct is mounted between two struts on a printed circuit board, and the leads are soldered to the necessary circuitry. In the case of solenoids with a stipulated inter-turn separation, the capillary may be replaced by a threaded former of appropriate pitch, and the wire wound in the threads. Alternatively, wire spacing may be maintained by simultaneously winding two wires

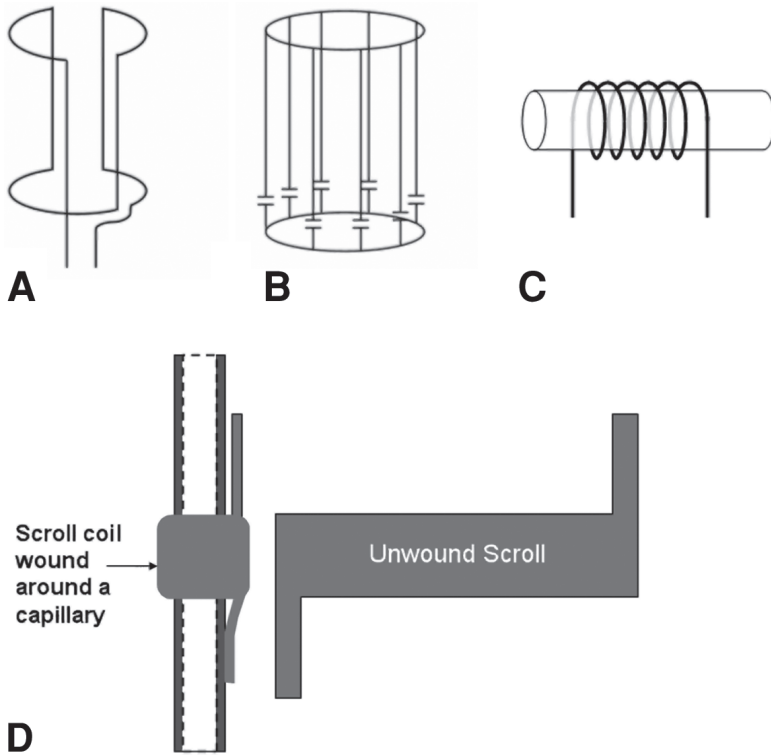


Fig. 2. Schematic drawings showing various configurations of radio frequency volume coils: (A) a saddle coil, (B) a birdcage coil, (C) a solenoid, and (D) the novel scroll geometry.

on the capillary and then unfurling one wire whose cross-sectional dimension is equal to the desired inter-turn spacing. Solenoid microcoils have been fabricated by winding thin wire on a micropipette tip while using a geared translational driver to achieve the necessary winding (16,17). Although the separation between the windings is difficult to control and reproduce, it is a critical factor in microcoil performance (18).

The performance of a single-layered solenoid is a function of the wire diameter, number of turns, inter-turn spacing, and aspect ratio (length:diameter). For the first approximation in the DC case, a solenoid's sensitivity at the center of the coil is:

$$\frac{B_1}{i} = \frac{\mu_0 \cdot n}{d \cdot \sqrt{1 + \left(\frac{l}{d}\right)^2}},$$

where  $\mu_0$  is the permeability of free space,  $n$  is the number of turns of the solenoid,  $d$  is the coil's diameter, and  $l$  is its length. The coil sensitivity increases inversely with  $d$ . However, in the microcoil regime, skin-effect losses play a dominant role in coil performance, and SNR improves inversely with  $d^{1/2}$  (7).  $B_1$  field homogeneity can be improved by winding a solenoid on a former that is nonuniform in its cross-section, or by varying the inter-turn spacing, thereby reducing field distortion from edge effects (19). Solenoid microcoils suffer from scalability and difficulty in fabrication. Wire thickness is a limiting factor in coil miniaturization, and multilayered solenoids are very difficult to wind. Scroll microcoils were developed to overcome these limitations (20,21)

A scroll microcoil (**Fig. 2**) is a conductor ribbon, laminated with a dielectric, and wound on itself to generate several sensing layers. Scroll microcoils can be fabricated from conductor sheets of thickness equal to twice the skin depth, and their dielectric layer makes them robust and easy to wind. A method for constructing scroll microcoils is detailed here. First, aluminum-backed copper sheets are laminated on the copper side with a dielectric polymer using vapor deposition. The aluminum backing is etched with sodium hydroxide and the copper–dielectric bilayer is used for patterning the microcoil and two leads with standard photolithography techniques. All subsequent steps of microcoil construction are similar to those described for the solenoid. Additional sensing layers of the scroll intensify the field and increase reception sensitivity up to a point, beyond which, the added resistance from incremental sensing layers outweighs the sensitivity gains, resulting in a drop in SNR.

SNR improvements of scrolls over solenoids were reported in a preliminary study by Gimi et al. (20). Although these SNR improvements are overestimated because the scroll design incorporated a sensing lead that contributed to signal, the basic approach is valid.

A major advantage of the scroll microcoil is that the  $B_1$  field homogeneity can be increased by varying the conductor pattern across the length of the microcoil to minimize edge effects, thereby eliminating the need to use a non-uniform capillary or former to achieve a similar effect, as is the case with the solenoid.

#### 2.1.3.1.1. Susceptibility Matching

The difference in magnetic susceptibility of the microcoil conductor and the surrounding air induces field distortion artefacts in the sample. To achieve high sensitivity, the filling factor must be maximized. A thin-walled capillary will allow sample proximity to the microcoil conductor, but makes the construct mechanically fragile and increases the penetration of susceptibility distortions into the sample. In imaging applications, the resultant line broadening may not

be detrimental to signal quality, but for high-resolution spectroscopy, a compromise must be made between sensitivity and resolution. To minimize these susceptibility artefacts, the conductor is surrounded by a material whose susceptibility closely matches that of the conductor.

#### 2.1.3.2. SURFACE MICROCOILS

The surface coil is the coil of choice for principally planar sample geometry because of high localized SNR in a plane proximal to the coil. The use of small samples in MR microscopy makes it very difficult to accurately place the sample within the sensing region of a volume microcoil. A surface microcoil provides ample space for sample placement and greater access to the sample for perfusion, manipulation, and replacement.

The spiral geometry is most commonly used in surface microcoils. As is the case with the scroll microcoil, additional turns of the spiral intensify the field generated, but as the number of conductor turns increases beyond an optimum number, the resistive losses from the additional turns overcome their contribution to SNR gain. Furthermore, with an augmenting spiral, the distance between the outer conductor trace and the sample region increases, progressively diminishing the outer turn's contribution to field strength. A plot of SNR per unit volume vs the number of spiral turns shows the optimal number of turns for a range of axial distance to starting radius ratios (**Fig. 3A**).

Taking advantage of photolithography and microfabrication techniques, the geometric parameters of a surface microcoil can be controlled with submicron resolution, and several microcoils can be fabricated on a single substrate. This section details two techniques used in fabricating surface microcoils, one that involves an easy approach to generating spiral microcoils with a starting radius upward of 750  $\mu\text{m}$ , and another that is more involved and robust and can be used for sub-500  $\mu\text{m}$  microcoils.

First, we discuss a straightforward method used to fabricate large spiral microcoils with starting radii upward of 750  $\mu\text{m}$  (**22**). Here, a double-sided, copper-clad Teflon substrate serves as a foundation for the microcoil, but the procedure can be easily adapted for any conductor and MR-compatible substrate. The spiral microcoil and main leads are patterned on one side using photolithography. The outer turn of the spiral is directly connected to one main lead. The inner turn of the spiral and the second lead are connected through a trace on the reverse side, using via holes to electroplate them to the trace. A strong electroplated connection through the via holes is critical, because this is a potential weak point in the circuit when delivering large currents to the microcoil. The assembly is laminated on 500  $\mu\text{m}$  Teflon for mechanical stability, and the microcoil is coated with a polymeric isolation layer. Such surface microcoils have been used in high-resolution imaging of implantable

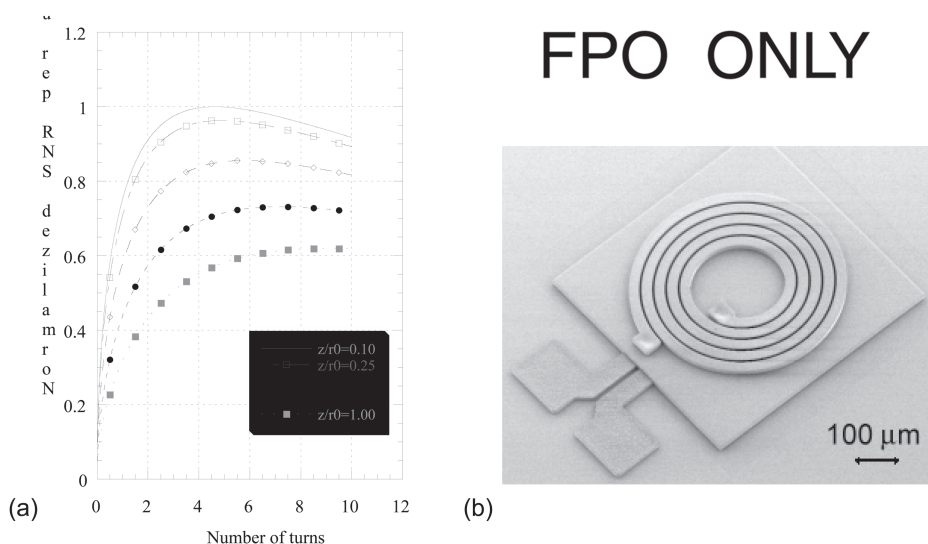


Fig. 3. (A) Normalized signal-to-noise ratio (SNR) per unit volume vs number of turns for a spiral coil with starting radius of 750  $\mu\text{m}$ ; trace width and inter-turn spacing, 100  $\mu\text{m}$ ; and trace width, 20  $\mu\text{m}$ . The figure shows that SNR increases with the number of turns of the spiral, up to a point, beyond which, the electrical losses in the circuit surmount the SNR gains from the additional turns. (Reproduced with permission from **ref. 22**.) (B) A scanning electron micrograph of spiral surface microcoil mold, showing the spiral conductor and the leads. (Reproduced with permission from **ref. 25**. © 2003 IEEE.)

biocapsules (23). The high-resolution images allow for investigating intracapsule cell distribution, viability, and diffusion and transport of nutrients and waste products. Surface microcoils have also been used in high-resolution imaging of intact pancreatic islets and *Xenopus laevis* oocytes (23) (**Fig. 4**). Easy replacement of the sample allows for the investigation of comparisons.

Another method used to generate a family of sub-500  $\mu\text{m}$  spiral microcoils involves electroplating copper into an SU-8 photoresist mold (24) (**Fig. 3B**). Copper leads are electroplated on a glass substrate and a 10- $\mu\text{m}$ -patterned SU-8 isolation layer is deposited to separate the leads from the microcoil. An additional seed layer is patterned, preceded by the deposition of a 55- $\mu\text{m}$  SU-8 mold. The microcoil spiral is constructed by depositing copper into the SU-8 mold. The leads are wire bonded to a printed circuit board on the RF probe, and embedded in epoxy for protection. Such microcoils were used to obtain high-resolution imaging of pancreatic islets and *Xenopus laevis* oocytes (25).

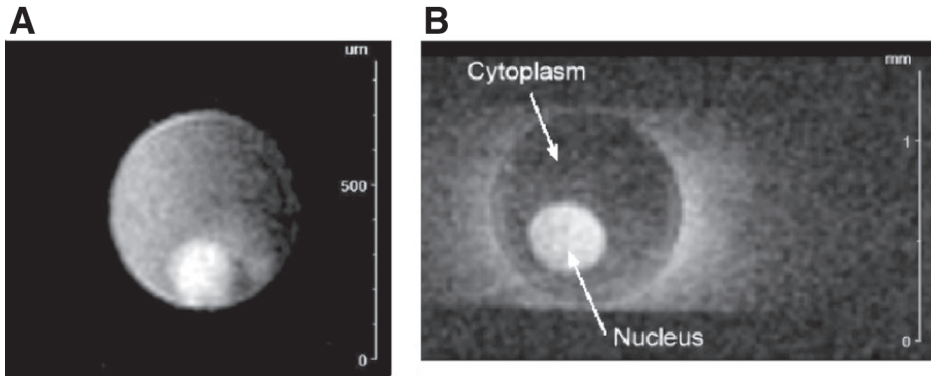


Fig. 4. (A) Image of a single islet of Langerhans with  $14\ \mu\text{m} \times 14\ \mu\text{m}$ , in-plane resolution on a  $100\text{-}\mu\text{m}$  slice. The standard spin-echo image was acquired with  $\text{TE} = 11.56\ \text{ms}$  and  $\text{TR} = 1200\ \text{ms}$ . (B) An image of an *Xenopus laevis* oocyte showing clear delineation between the nucleus and cytoplasm; gradient-echo image with  $\text{TR} = 300\ \text{ms}$ ,  $\text{TE} = 6.8\ \text{ms}$ ,  $16 \times 23 \times 100\ \mu\text{m}^3$  resolution, over a 1 h and 30 min acquisition. (Reproduced from **ref. 25** with permission. © 2003 IEEE.)

Although there can be no direct comparison between the sensitivity of volume coils and surface coils because surface coils have an ill-defined sensing volume, some broad comparisons are instructive in selecting a suitable coil for an experiment. Surface coils provide very high localized SNR, although their SNR advantage over volume coils decreases rapidly with increasing imaging distance from the plane of the coil (23). Surface coils generate radiant, inhomogeneous magnetic fields, resulting in spectral broadening. This obstacle can be avoided by imaging in a thin plane where the field is relatively homogeneous, correcting for  $B_1$  inhomogeneity during postprocessing, or using a Helmholtz configuration to increase the sensing region and RF homogeneity. To achieve high local SNR when imaging a large field-of-view, several surface microcoils may be used in a phased array (26). Parallel imaging techniques (27), such as sensitivity encoding (SENSE) (28) and simultaneous acquisition of spatial harmonics (SMASH) (29), are frequently employed in such applications (30,31). Chieh-Lin et al. (32) have shown that if the sample volume is fixed, an array of coils is preferred a single coil; whereas, if the sample can be scaled with the coil dimension, a single coil is preferred.

## 2.2. Technical Strategies: Gradients

The role of gradients in microscopy must be discussed in the context of diffusion, magnetic susceptibility, and the imaging sequence, all of which will be addressed in **Subheading 2.3**. In this section, we briefly discuss gradient

function, the need for strong gradients in microscopy, and hardware requirements and technical strategies to achieve efficient gradient operation. Sweeping through space with a magnetic field gradient results in spins at different points in space experiencing different local magnetic fields, which affects their precession frequency, which, in turn, reveals their spatial location. The stronger the gradient, the more accurate the spatial encoding, resulting in a direct correlation between gradient strength and spatial resolution. In addition, at high resolution, stronger and faster-switching gradients are required in MR microscopy to overcome signal degradation from broadening induced by susceptibility effects and molecular diffusion.

Effective gradients require high power, rapid switching, field homogeneity, and active shielding to prevent eddy current losses. The power requirements of strong gradients are achieved through very large pulsed currents with a high duty cycle; this sometimes requires custom-built power supplies to meet the current requirements and frequently requires external cooling. Overcoming signal loss through molecular diffusion requires rapid gradient switching. Seeber et al. (33) have achieved switching times as short as 10  $\mu$ s.

Gradient linearity, required for linear spatial encoding, is difficult to achieve over a large spatial region. Fortunately, microscopy requires gradient linearity over a small region of interest.

The changing magnetic flux from gradients generates eddy currents in other conducting structures, such as the magnetic bore, degrading SNR. Eddy currents may be reduced by actively shielded gradients or by using small gradient coils far from the magnetic bore.

Several approaches have been used to tackle these requirements and challenges of gradient design. Botwell and Robyrr (34) propose multilayered gradients with up to 650 W power dissipation. Zhang and Cory (35) demonstrate how fast-switching gradients of 600 T/m can be used in solid-state diffusion applications. Seeber et al. (36) have designed triple-axis gradients, as high as 50 T/m in one axis, capable of achieving approx 1 to 2  $\mu$ m resolution. As is evident from the proceeding sections, there are competing requirements on gradient strength and performance based on susceptibility and diffusion effects, involving trade-offs between resolution, SNR, and acquisition time (*see ref. 37 for further details*).

### **2.3. Phenomenological Strategies**

Resolving biological systems at the level of single cells and cellular clusters is critical to understanding the cellular response to perturbation and to discerning microscopic biochemical heterogeneity. The issue is not just that of resolution but also of information content. Contrast from cellular/subcellular boundaries and changes in relaxation times of the environment play a role in providing information about the biological system. MR signal and contrast

depends on the pulse sequence used to excite the sample and acquire the signal. Pulse sequences can be tailored to observe or highlight different physiological and functional phenomena, such as the structure and permeability of boundaries and interfaces, and molecular diffusion.

Several techniques are used to sensitize MR to tissue properties or tissue changes and are employed in microscopy. Cellular activation-based  $T_1$  weighting has been recently used in microscopy to study the function and viability of pancreatic  $\beta$ -cells, with paramagnetic  $Mn^{2+}$  as a  $T_1$  contrast agent (38,39).  $T_2$ -weighted microscopy exploits susceptibility effects to track stem-cell migration (40) and to observe immune responses in the central nervous system (41). Cobalt labeling has also been used in  $T_2$ -weighted microscopy to track nerve cell pathways (42). Fast spin-echo, high-field imaging has been developed for microscopy to increase imaging efficiency by reducing diffusion losses (43). Diffusion-weighted MR microscopy has shed light on compartmentalization of single neurons (44) and diffusion tensor imaging microscopy has been used to image the internal gray matter structure of the hippocampus, the thalamus, and the cortex (45). Chemical shift imaging techniques have tracked the metabolism of invading cells in cancer (46). Constant time imaging improves SNR when the gradient switching time is longer than  $T_2$  (47). The use of q-space imaging reveals cellular dimensions (48). Here, we accord susceptibility and diffusion effects more attention because they are salient to microscopy.

### 2.3.1. Susceptibility

MR spectral linewidth is defined as the full-width half maximum of a Lorentzian function, and is equal to:

$$\frac{1}{\pi \cdot T_2^*}.$$

Susceptibility mismatches create local field inhomogeneity and increase linewidth, resulting in signal attenuation from line broadening.

These susceptibility effects can be undesirable and can lead to poor image quality, or they can provide a valuable signature of the sample. Field distortions arising from cellular boundaries can be distinguished in gradient-echo experiments, providing a useful tool for microscopy of cell and tissue constructs.

#### 2.3.1.1. TECHNICAL STRATEGIES TO MINIMIZE SUSCEPTIBILITY-RELATED EFFECTS

For a given pixel, if the field variation caused by susceptibility is less than the variation caused by the gradient, susceptibility does not have an effect on image quality. Therefore, susceptibility effects are overcome by using large gradients, such that:

$$\frac{\Delta B_0}{\Delta r} \ll G ,$$

where  $\Delta B_0$  is the local variation in the magnetic field over a pixel of dimension  $\Delta r$ , and  $G$  is the strength of the gradient along that direction.

In the absence of diffusion effects, and only as a result of  $T_2$  and  $T_2^*$ :

$$\Delta r = \frac{1}{\gamma \cdot G \cdot \pi \cdot T_2^*} ,$$

where  $r \cdot \gamma \cdot G$  is the bandwidth.

Thus, increasing  $G$  will increase resolution, but SNR will decrease because of line broadening. It should be noted that there is a limit on resolution that is imposed by the bandwidth, expressed as:

$$(\Delta r)_{BW} = \frac{\Delta \phi^{min}}{\gamma \cdot G \cdot T} ,$$

where  $\phi^{min}$  is the minimum detectable phase and  $T$  is the signal acquisition time or the time of the applied phase encoding gradient (49). The minimum detectable phase is a function of the reconstruction algorithm and is equal to  $\pi$  for half-echo data in Fourier imaging. The above equation shows that bandwidth-limited resolution can be improved by increasing the signal acquisition time. Longer acquisition times are often undesirable because they involve loss of signal from molecular mobility, long breath holds, and prolonged anaesthesia. Therefore, increasing the gradient strength helps improve bandwidth-limited resolution.

When using phase-encoding sequences, longer echo times are required to allow for longer phase-encoding times, resulting in  $T_2$  signal loss. For a given reconstruction method, the bandwidth-limited resolution may be increased by increasing the gradient strength.

Susceptibility artefacts are rendered negligible by using several pulse sequences, for instance by employing a spin-echo sequence and acquiring images at the center of  $k$  space, where the refocusing of pixel distortion occurs. The gradient-echo sequence, on the other hand, will highlight contrast because of susceptibility effects.

### 2.3.1.2. SUSCEPTIBILITY AS A CONTRAST MECHANISM

Signal destruction by  $T_2$  and  $T_2^*$  effects creates hypointensity in weighted images.

Labeling cells with particles that induce susceptibility contrast is useful in tracking cell migration, homing, and biodistribution (50). MR detection of single cells is possible at low resolution by using large iron oxide particles to enhance susceptibility effects. Uptake of large iron oxide particles in mesenchymal stem cells and hematopoietic CD34<sup>+</sup> cells has exhibited very good T<sub>2</sub>\* contrast (51). Microscopy can detect single cells at high resolution, potentially reducing the doses of contrast agents.

Superparamagnetic monocrystalline iron oxide nanoparticles (MIONs) have been recently used to track stem cells and exhibit potential for sharp delineation of tumor borders. The rate of MION endocytosis in tumor cells exceeds that of normal cells, especially for cells at the tumor border, thus sharpening the tumor border in MR images. These MIONs have been used to image tumor cell endocytosis in vivo and ex vivo with microscopic resolution (52). Tumor border delineation has a potential application in the accurate estimation of tumor volume and in minimally invasive surgery. Therefore, susceptibility effects can deteriorate image quality or be used to track cells and image boundaries.

### 2.3.2. Diffusion

As is the case with susceptibility effects, signal loss caused by diffusion, blurring, and boundary artefacts are major challenges in microscopy, but signal loss and boundary artefacts can also be used to measure and deduce important biological information.

#### 2.3.2.1. TECHNICAL STRATEGIES TO MINIMIZE DIFFUSION-RELATED EFFECTS

Random Brownian motion results in some spins dispersing outside the voxel of interest. When spins disperse outside the voxel within the time of an acquisition they do not contribute to signal, resulting in low SNR. The diffusion-limited resolution is expressed as:

$$\Delta r_D = \sqrt{\frac{2}{3}DT_{acq}} ,$$

where  $\Delta r_D$  is the diffusion-limited spatial resolution,  $D$  is the coefficient of diffusion of the observed molecule, and  $T_{acq}$  is the acquisition time (49). Therefore, diffusion from random-phase fluctuation impedes on resolution only when the diffused distance is greater than the voxel dimension. Strong gradients can be applied to overcome phase dispersion and signal loss from diffusion.

Because time-varying signal attenuation has the effect of line broadening, resolution is adversely affected if the line broadening exceeds the voxel dimensions. This line-broadening effect is another limit on resolution because of

diffusion. For a given resolution and diffusion coefficient, the optimum acquisition time for maximum SNR is (53):

$$T_D^{opt} = \frac{3\Delta r^2}{2\pi^2 D}.$$

In both frequency- and phase-encoding sequences, large gradients are required to overcome diffusive attenuation, but in the phase-encoding case, the gradient strength does not adversely affect bandwidth. When diffusive attenuation in the read direction is a significant factor,  $T_2$  cannot be accurately measured by varying the echo time, TE. A Carr-Purcell-Meiboom-Gill pulse train is used to precede the echo sequence, providing  $T_2$  weighting. Other modified pulse sequences have been used to eliminate diffusion losses in microscopy (54).

### 2.3.2.2. DIFFUSION AS A CONTRAST MECHANISM

In some applications, diffusion effects must be compensated for, and, in others, diffusion effects can be used to provide a signature of the sample. For instance, diffusion near cell walls is limited, and manifests as boundary hyperintensity in the read direction. Fast and slow compartmental exchange are used to estimate cell size, membrane permeability, intracellular and extracellular volume fractions, and nuclear vs cytoplasmic signal contributions (55–57). Diffusion influences oxygen and nutrient gradients and bears on intercellular communication (58), making it a useful tool for the study of cellular microenvironment changes to local perturbation. Diffusion rates depend on the molecular environment as well as on restrictions that are either impermeable or partially permeable, and help distinguish physical and chemical domains.

The effective  $T_2$  relaxation time is a function of the true  $T_2$  relaxation time, as well as the b value, which, in turn, is a function of compartmentalization. The scenario is complicated by compartmentalization. Slow exchange will yield distinct values of  $T_2$  and the diffusion coefficient for each compartment, whereas fast exchange will yield a single value for the two parameters that is a weighted average of the components. These slow and fast exchange components can quantify membrane permeability, cell swelling and shrinkage, and the proliferation, destruction, and repopulation of cells in a tumor.

## 3. Applications

The effort toward MR microscopy is driven by the need to noninvasively detect molecular events, and to do so with high spatial localization and sufficient sensitivity to characterize low concentrations of metabolites. Investigators have used MR microscopy for high-resolution spectroscopy (11,13,59) and localized spectroscopy (60), as well as for microscopic imaging of cell and

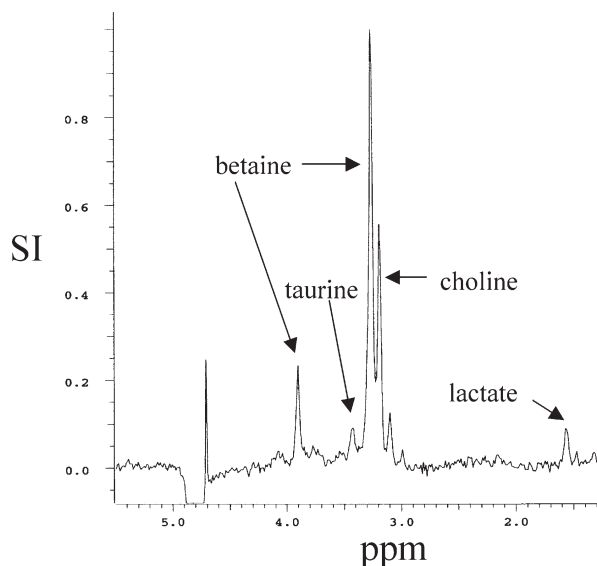


Fig. 5.  $^1\text{H}$  spectrum from a single neuron, averaged over 1 h and 40 m, shows betaine, taurine, and choline peaks, along with an emerging lactate peak. The spectrum was obtained from a  $220 \times 220 \times 220 \mu\text{m}^3$  voxel. The spectrum was acquired at 14 T, from a  $220 \mu\text{m} \times 220 \mu\text{m} \times 220 \mu\text{m}$  voxel. (From ref. 60. Copyright ©, 2000 Wiley InterScience. Reprinted by permission of Wiley-Liss, Inc., a subsidiary of John Wiley & Sons, Inc.)

tissue structures (61) and large single cells (10). Headway in cell tracking, single cell detection, and compartmental diffusion provides avenues to noninvasively study the molecular mechanism of disease onset and progression, and the response of cells and cellular structures to immune attack, gene therapy, and other perturbation.

### 3.1. Spectroscopy

With localized spectroscopy, NMR spectra of osmolytes and metabolites have been obtained from single neurons in concentrations on the order of tens of millimolar. **Figure 5** shows spectra from the L7 neuron of *Aplysia californica* taken every 8 min and averaged over 1 h and 40 min (60). These spectra were obtained from nanoliter volumes ( $220 \mu\text{m}$  isotropic voxel) using the stimulated echo acquisition mode (STEAM) sequence, and show betaine, taurine, and choline peaks, with the emergence of a lactate peak. Combined with single neuron microscopy in perfused systems (62), localized spectroscopy can be a potent tool in understanding the neuronal response to change in tonicity and other physiological perturbations.

### 3.2. Cellular Imaging and Compartmental Diffusion

MR microscopy is particularly well suited for imaging *Xenopus laevis* oocytes and embryos because light scattering from yolk inclusions severely impede optical imaging. Furthermore, intrinsic MR contrast can be used to identify the blastocoel (which has a higher water content than the rest of the embryo), and distinguishing the animal pole and the vegetal pole, the latter containing more fat. Sehy et al. (63) obtained high-resolution images of *Xenopus laevis* oocytes, measuring  $T_1$ ,  $T_2$ , and apparent diffusion coefficient (ADC) values. They measured ADC in the nucleus, the animal pole, and the vegetal pole of the oocyte, showing a higher ADC value in the animal pole compared with the vegetal pole, the latter containing less free water and more fat.

Schoeniger et al. (64) obtained proton density,  $T_1$ , and  $T_2$  images of single neurons of *Aplysia californica*. They also obtained diffusion coefficients from the nucleus and the cytoplasm, showing that proton diffusion in the nucleus was faster than in the cytoplasm. Similarly, Grant et al. (44) showed a higher ADC for the nucleus compared with the cytoplasm, using diffusion-weighted images.

### 3.3. Cellular Function

The noninvasive evaluation of tissue implants and transplants has emerged as a requisite for periodic evaluation of their function. To optimize implant and transplant function, one must thoroughly understand cellular response to drugs, immune attack, and other physiological perturbation. Transplanted pancreatic islets have emerged as a promising therapy for patients with type I diabetes. Given that a patient can be normoglycemic with as few as 2% of the native islets being functional, there is a clinical need to assess *in vivo* islet function to monitor and improve diabetes treatment. Manganese-enhanced MR microscopy of islet function was proposed by Gimi et al. (38,39) as an approach for the noninvasive *in vivo* scoring of islet activity. The islet microimaging study achieved  $14 \times 14 \mu\text{m}$  in-plane resolution on a  $100\text{-}\mu\text{m}$  slice over a 1 h and 36 min acquisition, with a standard spin-echo sequence. The study also performed MR microscopy on implantable biocapsules that encapsulate insulin-secreting  $\beta$ -cells. Although these high-resolution images are of value in studying the transplanted islets and implantable biocapsule, the system was designed to observe islet and  $\beta$ -cell activation maps. Much higher resolution is possible with further optimization of sample placement, using a more appropriate pulse sequence, and employing stronger gradients.

### 3.4. Embryonic Development and Multidimensional Animal Atlases

To gain insights into embryonic development and cell lineage, MR microscopy of single cells and cellular clusters must be evaluated in the context of the entire biological system. A multidimensional atlas of the embryo

can identify the genetic and molecular factors involved in embryonic development, and correlate morphological data to region-specific gene expression and biochemical data. (see **ref. 65** for a review). MR microscopy has a prominent role to play in the development of such atlases.

Jacobs and Fraser (**66**) longitudinally tracked cell motion and lineage of *Xenopus* embryos; Smith et al. (**67**) imaged fixed mouse embryos at different stages of development. MR microscopy was also employed in 3D angiography of fixed mouse embryos (**68**). Recently, Louie et al. (**69**) imaged gene expression in the *Xenopus* tadpole with a contrast agent that was enzymatically activated by removing its sugar cap from a water-coordinating site. Some of this work will be detailed later in the book.

### **3.5. Imaging Organ Microstructure and Function**

High-resolution MR has been employed in studying microscopic structure and function of the brain using standard imaging methods and contrast agents (**70,71**). Brain pathologies, including stroke, atrophy, dementia, hydrocephalus, and tumors have also been explored with MR microscopy (see **ref. 72** for an excellent review). Zhang et al. (**45**) have obtained high-resolution diffusion tensor images of the hippocampus, which is implicated in developmental and aging disorders, such as Down syndrome and Alzheimer's disease, respectively. Discovering microscopic anomalies and changes in neuronal architecture in the hippocampus will greatly aid in the understanding and early detection of these diseases. Although diffusion tensor microscopy does not achieve the resolution obtained through histology, the modality is less labor intensive than a three-dimensional histological reconstruction of the entire brain, and largely avoids sectioning artefacts, such as tissue deformation and loss. Therefore, diffusion tensor microscopy is not an alternative to histology but can be viewed as a noninvasive complementary technique that can be employed for rapid screening.

As mentioned previously, sample polarization enhances signal amplitude but is not always physiologically appropriate or possible. A notable exception is the use of hyperpolarized inert gas to image pulmonary microstructure and function, including pulmonary gas exchange, diffusion, and perfusion. Johnson et al. (**73**) have used the technique to discern airways down to the 7th branch.

## **4. Future**

### **4.1. Combining Optical Microscopy With MR**

Still within the realm of conventional MR microscopy, investigators have merged MR with optical microscopy to create an overlay of MR and optical images (**74,75**). Glover et al. (**74**) were the first to merge these two imaging modalities, imaging onion epidermal cells with 4.5- $\mu\text{m}$  in-plane resolution.

Wind et al. (75) used the technique to spatially register diffusion data from MR with organelle positions obtained from confocal images, showing a reduced diffusion rate in the region of mitochondrial clusters in a *Xenopus laevis* oocyte. Advances in integrated MR/optical systems will simultaneously yield high-resolution spatial resolution with high-resolution biochemical information.

#### 4.2. Magnetic Resonance Force Microscopy

Although technical improvements will incrementally increase resolution, new approaches may drastically change the landscape of MR microscopy. An emerging technique called magnetic resonance force microscopy (MRFM) uses force-detection MR instead of induction-detection MR; MRFM combines MR with conventional probe microscopy such as atomic force microscopy and scanning tunnel microscopy, and is capable of achieving atomic resolution on the order of 1 to 1000 Å (76,77).

The MR force microscope usually involves a cantilever with a ferromagnetic tip (magnetic field source) in close proximity to the sample. When an RF field is applied to the sample, the resulting magnetic moment in a small ensemble of spins generates a force on the cantilever, causing it to deflect. Resonance in the cantilever is achieved by modulating the RF field around the Larmor frequency, at the resonance frequency of the cantilever. The cantilever deflection is detected by an optical interferometer (Fig. 6).

In the system described above, natural field gradients (on the order of 10 G/nm) are generated by the ferromagnetic tip that is attached to the free end of the cantilever. In some cases, the sample is placed on the cantilever, with the ferromagnetic magnetic source is in close proximity to it. An alternate Better observation of magnetization, enhanced resolution, and no gradient (BOOMERANG) configuration places the detector magnet on the cantilever beam, with the sample being polarized. Here, the gradient is provided by the sample field, and the entire sample can be used for signal detection.]

Comparative studies show that MRFM provides sensitivity gains over conventional MR microscopy for small samples, such as membrane proteins, that are in close proximity to the cantilever (32). This sensitivity advantage increases as the nucleus gyromagnetic ratio decreases, further adding to the desirability of the technique. Even so, increasing distance from the cantilever results in loss of both sensitivity and gradient strength; for cell-sized samples, conventional MR microscopy is preferable to MRFM.

In conclusion, technological advances in microfabrication and nanofabrication; improved contrast techniques, such as targeted molecular probes and enzymatically amplified contrast; and the emergence of new technologies, such as MRFM and the integrated optical microscope/MR microscopes, are likely to carry microscopy into the realm where subcellular

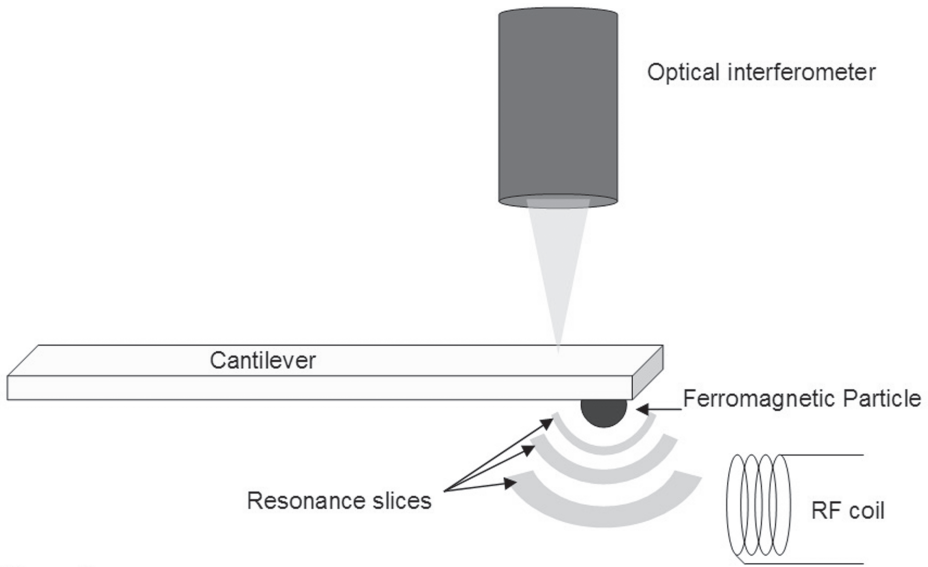


Fig. 6. A schematic of a magnetic resonance force microscope. The ferromagnetic particle generates magnetic field and a natural gradient. As the distance from the ferromagnetic particle increases, the magnetic gradient decreases and the resonance slice becomes thicker. Cantilever resonance is achieved by modulating the RF field around the Larmor frequency, at the resonant frequency of the cantilever. The interferometer measures the cantilever motion.

detection is routine. With developments in therapeutic implants and regenerative medicine, a greater push toward implantable coils is foreseeable for high-resolution, in vivo imaging. Integrating microfluidics with MR systems will prolong sample viability and provide the capability for dynamic perturbation of cellular and subcellular systems.

## Acknowledgments

I gratefully acknowledge Dr. Andrew Webb, Dr. Dmitri Artemov, Dr. Richard L. Magin, and Dr. Zaver Bhujwalla for important insights and support.

## References

1. Svensson, J., Mansson, S., Johansson, E., Petersson, J. S., and Olsson, L. E. (2003) Hyperpolarized  $^{13}\text{C}$  MR angiography using trueFISP. *Magn. Reson. Med.* **50**, 256–262.
2. Black, R. D., Early, T. A., Roemer, P. B., et al. (1993) A high-temperature superconducting receiver for nuclear magnetic resonance microscopy. *Science* **259**, 793–795.

3. Ginefri, J. C., Darrasse, L., and Crozat, P. (2001) High-temperature superconducting surface coil for in vivo microimaging of the human skin. *Magn. Reson. Med.* **45**, 376–382.
4. Hurlston, S. E., Brey, W. W., Suddarth, S. A., and Johnson, G. A. (1999) A high-temperature superconducting Helmholtz probe for microscopy at 9.4 T. *Magn. Reson. Med.* **41**, 1032–1038.
5. Wright, A. C., Song, H. K., and Wehrli, F. W. (2000) In vivo MR micro imaging with conventional radiofrequency coils cooled to 77K. *Mag. Reson. Med.* **43**, 163–169.
6. Hoult, D. I. and Richards, R. E. (1976) Signal-to-noise ratio of the nuclear magnetic-resonance experiment. *J. Magn. Reson.* **24**, 71–85.
7. Peck, T. L., Magin, R. L., and Lauterbur, P. C. (1995) Design and analysis of microcoils for NMR microscopy. *J. Magn. Reson. B* **108**, 114–124.
8. Hoult, D. I. and Lauterbur, P. C. (1979) The sensitivity of the zeugmatographic experiment involving human samples. *J. Magn. Reson.* **34**, 425–433.
9. Cho, Z. H., Ahn, C. B., Juh, S. C., et al. (1988) Nuclear magnetic resonance microscopy with 4-um resolution: theoretical study and experimental results. *Med. Phys.* **15**, 815.
10. Aguayo, J. B., Blackband, S. J., Schoeniger, J., Mattingly, M. A., and Hintermann, M. (1986) Nuclear magnetic resonance imaging of a single cell. *Nature* **322**, 190–191.
11. Olson, D. L., Peck, T. L., Webb, A. G., Magin, R. L., and Sweedler, J. V. (1995) High-resolution microcoil 1H-NMR for mass-limited, nanoliter-volume samples. *Science* **270**, 1967–1970.
12. Subramanian, R., Lam, M. M., and Webb, A. G. (1998) RF microcoil design for practical NMR of mass-limited samples. *J. Magn. Reson.* **133**, 227–231.
13. Subramanian, R. and Webb, A. G. (1998) Design of solenoidal microcoils for high-resolution <sup>13</sup>C NMR spectroscopy. *Anal. Chem.* **70**, 2454–2458.
14. Lee, S. C., Kim, K., Kim, J., et al. (2001) One micrometer resolution NMR microscopy. *J. Magn. Reson.* **150**, 207–213.
15. Webb, A. G. (1997) Radiofrequency microcoils in magnetic resonance. *Progress in Nuclear Magnetic Resonance Spectroscopy* **31**, 1–42.
16. Seeber, D. A., Cooper, R. L., Ciobanu, L., and Pennington, C. H. (2001) Design and testing of high sensitivity micro-receiver coil apparatus for nuclear magnetic resonance imaging. *Rev. Sci. Instrum.* **72**, 2171–2179.
17. Ciobanu, L., Seeber, D. A., and Pennington, C. H. (2002) 3D MR microscopy with resolution 3.7 micron by 3.3 micron by 3.3 micron. *J. Magn. Reson.* **158**, 178–182.
18. Peck, T. L. (1992) Ph.D. dissertation. University of Illinois at Urbana/Champaign, IL.
19. Idziak, S. and Haerberlen, U. (1982) *J. Magn. Reson.* **50**, 281.
20. Gimi, B., Grant, S. C., Magin, R. L., Fienerman, A., Frolova, E., and Friedman, G. (2000) SNR improvements for RF scroll microcoils. *Experimental Nuclear Magnetic Resonance Conference*. Asilomar, CA. April 2000.
21. Gimi, B., Grant, S. C., Magin, R. L., and Friedman, G. (2000) Investigation of NMR signal-to-noise for RF scroll microcoils. *Proceedings of 1st Annual International IEEE-EMBS Special Topics Conference on Microtechnologies in Medicine & Biology*. Oct. 2000, Lyons, France.

22. Eroglu, S., Gimi, B., Roman, B., Friedman, G., and Magin, R. L. (2003) NMR spiral surface microcoils: field characteristics and applications. *Concepts in Magnetic Resonance Imaging Part B*, **17B**(1), 1–10.
23. Gimi, B., Eroglu, S., Leoni, L., Desai, T. A., Magin, R. L., and Roman, B. (2003) NMR spiral surface microcoils: applications. *Concepts in Magnetic Resonance Imaging Part B*, **18B**(1), 189–200.
24. Massin, C., Boero, G., Vincent, F., Abenheim, J., Besse, P.-A., and Popovic, R. S. (2002) High-Q factor RF planar microcoils for micro-scale NMR spectroscopy. *Sens. Actuators A Phys.* **97–98**, 280–288.
25. Massin, C., Eroglu, S., Vincent, F., et al. (2003) Planar microcoil-based magnetic resonance imaging of cells. Proceedings of *Transducers '03*, Boston, MA, June, 2003, 967–970.
26. Roemer, P. B., Edelstein, W. A., Hayes, C. E., Souza, S. P., and Mueller, O. M. (1990) The NMR phased array. *Magn. Reson. Med.* **16**, 192–225.
27. Sodickson, D. K. and McKenzie, C. A. (2001) A generalized approach to parallel magnetic resonance imaging. *Med. Phys.* **28**, 1629–1643.
28. Wright, S. M., Magin, R. L., and Kelton, J. R. (1991) Arrays of mutually coupled receiver coils: theory and application. *Magn. Reson. Med.* **17**, 252–268.
29. Sodickson, D. K. and Manning, W. J. (1997) Simultaneous acquisition of spatial harmonics (SMASH): fast imaging with radiofrequency coil arrays. *Magn. Reson. Med.* **38**, 591–603.
30. Pruessmann, K. P., Weiger, M., Scheidegger, M. B., and Boesiger, P. (1999) SENSE: sensitivity encoding for fast MRI. *Magn. Reson. Med.* **42**, 952–962.
31. Sodickson, D. K., McKenzie, C. A., Ohliger, M. A., Yeh, E. N., and Price, M. D. (2002) Recent advances in image reconstruction, coil sensitivity calibration, and coil array design for SMASH and generalized parallel MRI. *Magma* **13**, 158–163.
32. Lin, W.-C. and Fedder, G. K. (2001) *A Comparison of Induction-Detection NMR and Force-Detection NMR on Micro-NMR Device Design*. The Robotics Institute of Computer Science, Carnegie Mellon University, Pittsburgh, PA.
33. Seeber, D. A., Hoftiezer, J. H., and Pennington, C. H. (2002) Pulsed current gradient power supply for microcoil magnetic resonance imaging. *Concepts in Magnetic Resonance Imaging Part B* **15**, 189.
34. Bowtell, R. and Robyr, P. (1998) *J. Magn. Reson.* **131**, 286–294.
35. Zhang, H. and Cory, D. G. (1998) Pulsed gradient NMR probes for solid state studies. *J. Magn. Reson.* **132**, 144–149.
36. Seeber, D. A., Hoftiezer, J. H., Daniel, W. B., Rutgers, M. A., and Pennington, C. H. (2000) Triaxial magnetic field gradient system for microcoil magnetic resonance imaging. *Rev. Sci. Instrum.* **71**, 4263–4272.
37. Glover, P. M. and Mansfield, P. (2002) Limits to magnetic resonance microscopy. *Rep. Prog. Phys.* **65**, 1489–1511.
38. Gimi, B., Leoni, L., Braun, M., Eroglu, S., Magin, R. L., and Roman, B. (2003) Non-invasive functional microimaging of pancreatic islets using manganese enhanced MRI. *The Society for Molecular Imaging, Second Annual Meeting*. San Francisco, CA, Aug, 2003.

39. Gimi, B., Leoni, L., Eroglu, S., Desai, T. A., Magin, R. L., and Roman, B. (2002) Non-invasive monitoring of encapsulated beta cell function using Mn<sup>2+</sup>-enhanced magnetic resonance imaging. *Second Annual Diabetes Technology Meeting, Atlanta, GA, Oct.–Nov., 2002.*
40. Bulte, J. W., Douglas, T., Witwer, B., et al. (2001) Magnetodendrimers allow endosomal magnetic labeling and in vivo tracking of stem cells. *Nat. Biotechnol.* **19**, 1141–1147.
41. Dousset, V., Delalande, C., Ballarino, L., et al. (1999) In vivo macrophage activity imaging in the central nervous system detected by magnetic resonance. *Magn. Reson. Med.* **41**, 329–333.
42. Quast, M. J., Neumeister, H., Ezell, E. L., and Budelmann, B. U. (2001) MR microscopy of cobalt-labeled nerve cells and pathways in an invertebrate brain (*Sepia officinalis*, Cephalopoda). *Magn. Reson. Med.* **45**, 575–579.
43. Zhou, X., Cofer, G. P., Suddarth, S. A., and Johnson, G. A. (1993) High-field MR microscopy using fast spin-echoes. *Magn. Reson. Med.* **30**, 60–67.
44. Grant, S. C., Buckley, D. L., Gibbs, S., Webb, A. G., and Blackband, S. J. (2001) MR microscopy of multicomponent diffusion in single neurons. *Magn. Reson. Med.* **46**, 1107–1112.
45. Zhang, J., van Zijl, P. C., and Mori, S. (2002) Three-dimensional diffusion tensor magnetic resonance microimaging of adult mouse brain and hippocampus. *Neuroimage* **15**, 892–901.
46. Artemov, D., Pilatus, U., Chu, S., Mori, N., Nelson, J. B., and Bhujwala, Z. M. (1999) Dynamics of prostate cancer cell invasion studied in vitro by NMR microscopy. *Magn. Reson. Med.* **42**, 277–282.
47. Gravina, S. and Cory, D. G. (1994) Sensitivity and resolution of constant-time imaging. *J. Magn. Reson. Series B* **104**, 53–61.
48. Cohen, Y. and Assaf, Y. (2002) High b-value q-space analyzed diffusion-weighted MRS and MRI in neuronal tissues—a technical review. *NMR Biomed.* **15**, 516–542.
49. Cho, Z. H., Lee, S. C., and Cho, M. H. *NMR Microscopy: Resolution, in: Methods in Biomedical Magnetic Resonance Imaging and Spectroscopy* (Young, I., ed.), John Wiley & Sons, pp. 433–439.
50. Gimi, B., Mori, N., Ackerstaff, E., Frost, E. E., Bulte, J. W. M., and Bhujwala, Z. M. (2004) MR imaging of superparamagnetically labeled endothelial cells revealed directed migration in response to factors secreted by human breast cancer cells. *The Third Annual Meeting of the Society for Molecular Imaging*. St. Louis, MO., Sept. 2004.
51. Hinds, K. A., Hill, J. M., Shapiro, et al. (2003) Highly efficient endosomal labeling of progenitor and stem cells with large magnetic particles allows magnetic resonance imaging of single cells. *Blood* **102**, 867–872.
52. Zimmer, C., Wright, S. C., Jr., Engelhardt, R. T., et al. (1997) Tumor cell endocytosis imaging facilitates delineation of the glioma-brain interface. *Exp. Neurol.* **143**, 61–69.
53. Cho, Z. H., Ahn, C. B., Juh, S. C., et al. (1988) Nuclear magnetic resonance microscopy with 4-microns resolution: theoretical study and experimental results. *Med. Phys.* **15**, 815–824.

54. Hsu, E. W., Schoeniger, J. S., Bowtell, R., Aiken, N. R., Horsman, A., and Blackband, S. J. (1995) A modified imaging sequence for accurate T2 measurements using NMR microscopy. *J. Magn. Reson. B* **109**, 66–69.
55. Duong, T. Q., Sehy, J. V., Yablonskiy, D. A., Snider, B. J., Ackerman, J. J., and Neil, J. J. (2001) Extracellular apparent diffusion in rat brain. *Magn. Reson. Med.* **45**, 801–810.
56. Sehy, J. V., Banks, A. A., Ackerman, J. J., and Neil, J. J. (2002) Importance of intracellular water apparent diffusion to the measurement of membrane permeability. *Biophys. J.* **83**, 2856–2863.
57. Sehy, J. V., Ackerman, J. J., and Neil, J. J. (2002) Evidence that both fast and slow water ADC components arise from intracellular space. *Magn. Reson. Med.* **48**, 765–770.
58. Francis, K. and Palsson, B. O. (1997) Effective intercellular communication distances are determined by the relative time constants for cyto/chemokine secretion and diffusion. *Proc. Natl. Acad. Sci. USA* **94**, 12,258–12,262.
59. Minard, K. R. and Wind, R. A. (2002) Picoliter (1)H NMR spectroscopy. *J. Magn. Reson.* **154**, 336–343.
60. Grant, S. C., Aiken, N. R., Plant, H. D., et al. (2000) NMR spectroscopy of single neurons. *Mag. Reson. Med.* **44**, 19–22.
61. Cho, Z. H., Ahn, C. B., Juh, S. C., et al. (1990) Recent progress in NMR microscopy toward cellular imaging. *Trans. Royal Soc. London* **333**, 469–475.
62. Hsu, E. W., Aiken, N. R., and Blackband, S. J. (1996) Nuclear magnetic resonance microscopy of single neurons under hypotonic perturbation. *Am. J. Physiol.* **271**, C1895–C1900.
63. Sehy, J. V., Ackerman, J. J., and Neil, J. J. (2001) Water and lipid MRI of the *Xenopus* oocyte. *Magn. Reson. Med.* **46**, 900–906.
64. Schoeniger, J. S., Aiken, N., Hsu, E., and Blackband, S. J. (1994) Relaxation-time and diffusion NMR microscopy of single neurons. *J. Magn. Reson. B* **103**, 261–273.
65. Jacobs, R. E., Papan, C., Ruffins, S., Tyszka, J. M., and Fraser, S. E. (2003) MRI: volumetric imaging for vital imaging and atlas construction. *Nat. Rev. Mol. Cell. Biol.* **4** (Suppl). SS10–SS16.
66. Jacobs, R. E. and Fraser, S. E. (1994) Magnetic resonance microscopy of embryonic cell lineages and movements. *Science* **263**, 681–684.
67. Smith, B. R., Linney, E., Huff, D. S., and Johnson, G. A. (1996) Magnetic resonance microscopy of embryos. *Comput. Med. Imaging Graph.* **20**, 483–490.
68. Smith, B. R., Johnson, G. A., Groman, E. V., and Linney, E. (1994) Magnetic resonance microscopy of mouse embryos. *Proc. Natl. Acad. Sci. USA* **91**, 3530–3533.
69. Louie, A. Y., Huber, M. M., Ahrens, E. T., et al. (2000) In vivo visualization of gene expression using magnetic resonance imaging. *Nat. Biotechnol.* **18**, 321–325.
70. Johnson, G. A., Benveniste, H., Engelhardt, R. T., Qiu, H., and Hedlund, L. W. (1997) Magnetic resonance microscopy in basic studies of brain structure and function. *Ann. N. Y. Acad. Sci.* **820**, 139–147; discussion 147–148.
71. Ahrens, E. T., Laidlaw, D. H., Readhead, C., Brosnan, C. F., Fraser, S. E., and Jacobs, R. E. (1998) MR microscopy of transgenic mice that spontaneously acquire experimental allergic encephalomyelitis. *Magn. Reson. Med.* **40**, 119–132.

72. Benveniste, H. and Blackband, S. (2002) MR microscopy and high resolution small animal MRI: applications in neuroscience research. *Prog. Neurobiol.* **67**, 393–420.
73. Johnson, G. A., Cofer, G. P., Hedlund, L. W., Maronport, R. R., and Suddarth, S. A. (2001) Registered H-1 and He-3 magnetic resonance microscopy of the lung. *Mag. Reson. Med.* **45**, 365–370.
74. Glover, P. M., Bowtell, R. W., Brown, G. D., and Mansfield, P. (1994) A microscope slide probe for high resolution imaging at 11.7 Tesla. *Magn. Reson. Med.* **31**, 423–428.
75. Wind, R. A., Minard, K. R., Holtom, G. R., et al. (2000) An integrated confocal and magnetic resonance microscope for cellular research. *J. Magn. Reson.* **147**, 371–377.
76. Sidles, J. A. and Rugar, D. (1993) Signal-to-noise ratios in inductive and mechanical detection of magnetic resonance. *Phys. Rev. Lett* **70**, 3506–3509.
77. Schaff, A. and Veeman, W. S. (1997) Mechanically detected nuclear magnetic resonance at room temperature and normal pressure. *J. Magn. Reson.* **126**, 200–206.



<http://www.springer.com/978-1-58829-397-8>

Magnetic Resonance Imaging  
Methods and Biologic Applications

Prasad, P.V. (Ed.)

2006, XV, 447 p., Hardcover

ISBN: 978-1-58829-397-8

A product of Humana Press